# Dynamic power response shaping using adaptive constraints in feedback control of a contra-rotating pump–turbine

Truijen, Daan P.K.; Ansorena Ruiz, Ruben; Hoffstaedt, Justus; Schürenkamp, David; Goseberg, Nils; Jarquin Laguna, Antonio; Stockman, Kurt; De Kooning, Jeroen D.M.

**DOI**
10.1016/j.energy.2025.136753

**Publication date**
2025

**Document Version**
Final published version

**Published in**
Energy

Energy 331 (2025) 136753

Contents lists available at ScienceDirect

Energy

journal homepage: www.elsevier.com/locate/energy

# Dynamic power response shaping using adaptive constraints in feedback control of a contra-rotating pump–turbine

Daan P.K. Truijen [a,b,*], Ruben Ansorena Ruiz [c], Justus Hoffstaedt [e], David Schürenkamp [c], Nils Goseberg [c,d], Antonio Jarquin Laguna [e], Kurt Stockman [a,b], Jeroen D.M. De Kooning [a,b]

[a] Department of Electromechanical, Systems & Metal Engineering, Ghent University, Sint-Martens-Latemlaan 2B, 8500, Kortrijk, Belgium
[b] FlandersMake@UGent - Corelab MIRO, Belgium
[c] Leichtweiß-Institute for Hydraulic Engineering and Water Resources, Technische Universität Braunschweig, Beethovenstraße 51A, 38106, Braunschweig, Germany
[d] Coastal Research Center Joint Research Facility of Leibniz University Hannover and Technische Universität Hannover, Merkurstraße 11, 30419, Hannover, Germany
[e] Department of Maritime and Transport Technology, Delft University of Technology, Mekelweg 2, 2628 CD, Delft, The Netherlands

## ARTICLE INFO

*Keywords:*
Hydropower storage
Contra-rotating pump–turbine
Frequency containment reserve
Response shaping
Turbine efficiency

## ABSTRACT

With the rising need for flexible energy storage, recent research shows the potential of contra-rotating reversible pump–turbines (CR RPT) to enable low-head pumped hydropower storage. This study presents a dual variable-speed control architecture for CR RPTs, aimed at providing grid frequency control. The proposed control maximizes the efficiency and shapes the power response to minimize the rise time while averting excessive fluctuations. The control architecture is experimentally validated on a 45 kW reduced-scale CR RPT. The results show that for full reserve activation in frequency containment reserve (FCR), the rise times are $< 3.92$ s in turbine mode and $< 0.23$ s in pump mode. When scaled to a 10 MW system, with a factor of 1.53 to 2.46, the rise times remain well below the regulatory limit of 30 s. Furthermore, the power response stays within the allowed limits, with root mean square deviations of $< 58\%$ in turbine mode and $< 39\%$ in pump mode, relative to the allowed limits. Additionally, the system effectively tracks the varying power setpoints in an actual FCR use case. These findings demonstrate that the proposed control methodology can successfully provide frequency control by dynamically varying the power within imposed power constraints.

## 1. Introduction

In the past decade, the global adoption of renewable energy sources has surged, increasing their share of global power generation from under 20% in 2010 to 30.2% in 2023 [1]. Wind energy and photovoltaic (PV) technologies have experienced the most significant growth, with their share of generated electricity rising from 2.8% and 0.6% respectively in 2013 to 7.8% and 5.4% in 2023. By 2028, their energy shares are expected to increase to respectively 12.1% and 12.6% [1]. As the penetration of these intermittent and non-dispatchable energy sources increases, they partially replace the traditional high-inertia and dispatchable energy sources. Therefore, energy storage systems are becoming increasingly indispensable for maintaining the reliability and stability of power systems. Among the various energy storage systems, pumped hydropower storage (PHS) is the most cost-effective [2] due to its long lifetime. It accounts for more than 90% of global energy storage, with an installed capacity of 160 GW [3]. In addition to compensating for seasonal and hourly fluctuations, dynamic storage systems are required to support the grid frequency through frequency reserves. Among these, frequency containment reserve (FCR) is a dynamic reserve that is applied worldwide. In FCR, the power is automatically and linearly adjusted to the grid frequency deviation, with the full reserve activation time ensured to be below 30 s [4]. To account for this short term storage, mostly grid-scale electrochemical batteries have been installed in the last decade, with an installed capacity of 28 GW in 2022 [3]. Furthermore, to facilitate the increased penetration of renewable energy sources, the installed short-term storage is expected to increase by > 400 GW by 2028 [1]. Although it is generally expected that batteries will fill this gap, it has been shown that variable-speed

* Corresponding author at: Department of Electromechanical, Systems & Metal Engineering, Ghent University, Sint-Martens-Latemlaan 2B, 8500, Kortrijk, Belgium.
*E-mail addresses:* daan.truijen@ugent.be (D.P.K. Truijen), r.ansorena-ruiz@tu-braunschweig.de (R. Ansorena Ruiz), j.p.hoffstaedt@tudelft.nl (J. Hoffstaedt), jeroen.dekooning@ugent.be (J.D.M. De Kooning).

https://doi.org/10.1016/j.energy.2025.136753
Received 10 October 2024; Received in revised form 4 March 2025; Accepted 21 May 2025
Available online 7 June 2025

PHS systems can also be used to provide frequency reserves, with over 90% of all FCR performed by hydropower systems during the frequency containment project in the Nordic regional group ending in 2016 [5]. However, it has to be noted that the dynamic requirements have since increased, and grid-scale battery costs have decreased.

This increased necessity for energy storage initiated investigations into low-head PHS, which, in contrast to its traditional high-head counterpart, is not restricted to mountainous regions, and can be installed in run-of-river systems or shallow seas [6]. In [7], a novel contra-rotating reversible pump–turbine (CR RPT) was developed. This RPT features two runners rotating in opposite directions, which minimizes swirl development and allows to retain a high efficiency in low-head, high-flow systems. As this RPT has two runners, two degrees of freedom with a dynamic coupling through the fluid dynamics are available in the control system. Therefore, the question arises as to how the control architecture can exploit this dual variable-speed system to participate in frequency control. As most traditional hydropower systems use a power take-off comprising grid-coupled synchronous machines, the FCR power response was initially enabled by inlet vane or governor control, with multiple studies on PID-based power control available in literature [8–11]. Furthermore, recent studies apply a sliding mode controller [12] and model predictive control (MPC) [13–15]. However, the implementation of fully rated converters with variable-speed motor-generators allows to increase the dynamic power response, the operating range, and efficiency at off-design operating points [16]. In [17,18], a PID-based power control is proposed through torque control in pump mode. However, this methodology cannot be applied in turbine mode, as a change in torque inversely affects the rotational speed and power (after an initial inertial power response). Multiple studies propose to solve this drawback by restoring the rotational speed after the inertial response by controlling the flow rate using governor control [19–22]. Although the power response is fast, the algorithm does not operate at the optimal efficiency point. Furthermore, power stability is guaranteed only if the water column and governor inertia are significantly lower than the mechanical inertia of the turbine, and the power steps are limited [22]. Iterative extremum-seeking control algorithms have been developed through perturb-and-observe [23–25], fuzzy control based on perturb-and-observe [26], and gradient descent [27,28] algorithms. However, their iterative nature significantly limits the dynamic power response. Next, in [29], a lookup table based on a 1D Euler model stores the rotational speed that reaches the highest efficiency for a range of power setpoints, where this rotational speed is realized through PID control. However, in this case, the derived dynamic response is not optimized and suffers from fluctuations. In [30,31], it is shown how variable-speed model predictive control (MPC) of a high-head single-runner turbine can provide ancillary services to the electrical grid. In [32], an MPC controller is developed for a Francis-type pump–turbine, with the increase in performance of MPC compared to a power PID controller analyzed in [33]. However, in MPC controllers, the fidelity of the dynamic model significantly affects the controller performance and stability [34]. In the used models (based on Euler equations [30,31,33]), e.g. viscous effects – comprising flow separation, tip clearance effects, and turbulence – are not included, while these effects become prominent in dynamic operation, which can result in decreased performance and instability.

An overview of the existing variable-speed power control algorithms is presented in Table 1. The contributions of this study to the literature are threefold:

- First, a novel dual variable-speed lookup table-based control architecture is presented that aims to maximize the efficiency and power response rise time of a dual rotor CR RPT in a low-head PHS system. Existing algorithms such as power PID and perturb and observe are not inherently suited for dual rotor systems, while gradient descent requires an accurate estimation of the gradient to be effective.

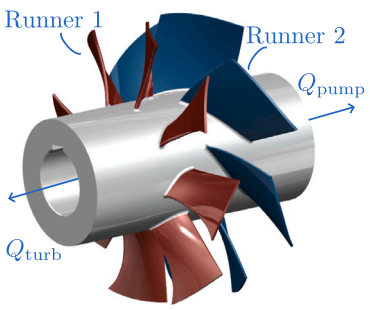


**Fig. 1.** CAD render of the reduced-scale CR RPT.

- Second, a method to shape the power response through torque constraints has not been explored. The main novelty of this study comprises the dynamic power response shaping, which is implemented using adaptive torque constraints, enabling the system to participate in frequency control. Depending on the type of frequency control and local regulations, the power can be shaped accordingly by tuning the torque constraints.
- Third, although MPC can also constrain the power fluctuations, dynamic effects in hydropower pump–turbines are complex and computationally expensive to capture in a predictive model. To the best of the authors' knowledge, these algorithms have not been validated thus far. In this study, the developed control architecture is validated experimentally with the dynamic requirements of FCR on a model scale 45 kW CR RPT in a test-setup with two open reservoirs, optimally replicating a real operating environment. Although FCR requires a rise time of $< 30$ s, the control architecture aims to minimize the rise time without exceeding the power constraints.

In Section 2, the system and test-setup are outlined in Section 2.1 and characterized in Section 2.2. Next, the research methodology is outlined in Section 3, comprising the control architecture and the power response criteria for FCR. Finally, the experimental validation of the system performing FCR is outlined in Section 4.

## 2. System description and characterization

### 2.1. System description and experimental setup

Fig. 1 shows a CAD render of the CR RPT. This CR RPT is a scaled version (1:20.58) with geometric similarity of a 10 MW prototype with a diameter of 5.68 m [6]. Here, the affinity laws are applied to scale the RPT diameter so that the flow coefficient, head coefficient and power coefficient are equal in prototype and model scale [35]. The CR-RPT has two variable-speed runners that rotate in opposite directions, minimizing swirl development and maintaining high efficiency in a low-head high-flow system [16,36]. The two runners are highly coupled through their interaction with the fluid, as the inlet flow of the downstream runner is deflected by the upstream runner. To quantify this interaction between the two runners, multiple computational fluid dynamics studies have been performed in literature [7,37,38], where the influence of nonlinear effects, such as flow separation and swirl development between the runners, is highlighted.

Fig. 2(a) provides a schematic overview of the test-setup, which comprises two open surface reservoirs [39]. These large reservoirs avert the use of a pump to achieve hydraulic head, mitigating the accessory impact on flow uniformity and pressure fluctuations. The water levels of the lower and elevated tank are respectively $h_{s1} = 2.28$ m and $h_{s2} = 10.08$ m above the centerline of the RPT, resulting in a steady gross hydraulic head of $\Delta h = 7.8$ m. The conduit has a diameter of 50 cm, tapering to 27.6 cm via the two contraction/expansion tubes

**Table 1**
Overview of existing variable-speed power control algorithms for hydropower pump–turbines.

| Algorithm/Reference | Power response | Power fluctuations | Exp. validation | Discussion |
|---|---|---|---|---|
| Power PID [17,18] | Fast | Small | ✗ | - Not suitable for turbine mode |
| Power PID + Speed PID [19–22] | Fast | Small | ✗ | - Suboptimal efficiency<br>- Possible stability issues based on inertia<br>- Limited power step.<br>- Not suitable for dual-rotor systems |
| Perturb and Observe [23–26] | Slow | Large | ✓ | - Iterative nature limits dynamic response<br>- Step size trade-off between power response and fluctuations<br>- Not suitable for multiple parameter systems |
| Gradient descent [27,28] | Slow | Large | ✓ | - Learning rate trade-off between power response and fluctuations<br>- Accurate estimation of gradient imperative for multiple parameter systems. |
| Lookup table-based [29] | Fast | Large | ✗ | - Requires an accurate (static) model |
| MPC [30–33] | Fast | Constrained | ✗ | - Computationally expensive<br>- Requires an accurate dynamic model<br>- Model inaccuracies can lead to decreased performance and instability |

**Table 2**
List of the used instrumentation.

| Measurement | Instrumentation | Range | Accuracy |
|---|---|---|---|
| Flow — $Q$ | Krohne OPTIFLUX 2000 | 0–600 l/s | 0.20% + 0.2 l/s |
| Pressure — $p_{1,3}$ | Druck Limited PDCR 1830 | −0.5–0.35 bar | 0.1% |
| Pressure — $p_2$ | BD Sensors DMP 321 | 0–2.4 bar | 0.25% |
| Torque — $\tau_{s1,2}$ | HBM T22 | 0–500 N m | 0.5% |
| Rot. speed — $\omega_{1,2}$ | SICK DBS60 | 0–9000 rpm | 0.015% |

next to the RPT. A butterfly valve, positioned between the elevated tank and the RPT is used in start-up and shut-down scenarios. In this setup, a steady water level in both tanks is ensured by installing spillways that allow water to overflow to an underground reservoir. As seen in Fig. 2(b), each runner of the RPT is separately driven by a 32 kW axial-flux permanent magnet synchronous machine (AF-PMSM), coupled to a fully regenerative ABB ACS880 variable-frequency drive. This allows independent variable-speed control of the RPT runners. To connect the runners to the PMSMs, two sets of bevel gears (ratio 1:1) are integrated into the hubs on each side of the RPT. Note that for the full-scale system, bevel gears are avoided and bulbs inside the conduit are proposed instead [40]. To visually assess cavitation, the RPT is surrounded by an acrylic glass tube. The sensor locations are illustrated in Fig. 2 and their specifications are listed in Table 2 [39]. Two pressure probes $p_{1,2}$ are placed on either side of the RPT, with a third probe $p_3$ placed before the conduit contraction at the low-pressure side. An electromagnetic flow meter is used to minimize interference. The torques and rotational speeds are measured using two torque transducers and two incremental encoders, respectively, positioned in series with the AF-PMSMs.

To assess whether the dynamic experiments on this reduced-scale test-setup can provide an indication of the dynamic performance of the full-scale 10 MW system, the two main inertia constants of a hydropower system are compared: the mechanical inertia constant $H_m$ and the water inertia constant $H_w$ [27]:

$$H_m = \frac{1}{2}\frac{J \cdot \omega_N}{\tau_N} \tag{1}$$

$$H_w = \frac{L_c}{g \cdot A_c}\frac{Q_N}{\Delta h_N}, \tag{2}$$

where $J$ is the rotational inertia, and $L$ and $A_c$ are the length and area of the conduit, respectively. The quantities $\omega_N, \tau_N, Q_N$, and $\Delta h_N$ are the nominal rotational speed, torque, flow rate, and fallhead, respectively.

The main parameters for both the full-scale and the reduced-scale (1:20.58) systems are listed in Table 3. Here, the rotational inertia comprises the runner, shaft, and machine inertia. For all three inertia constants, the constants are higher for the full-scale system. The ratios $H_{m,w}^{\text{full-scale}}/H_{m,w}^{\text{scaled}}$ are 1.70, 1.53, and 2.46 for the mechanical inertia constant for runner 1 and runner 2, and the water inertia constant, respectively. Therefore, the experimental results in this study can give an indication of the dynamics of the full-scale system by multiplying the power rise time with a factor between 1.53 and 2.46. Note that this factor is based only on the inertia constants, with other scaling effects not included [41]. Although careful consideration was given to these factors during the manufacturing process, a relatively increased surface roughness and tip clearance compared to the full-scale system are factors that can limit the performance despite the geometric similarity [35,42]. In order to limit the viscous effects in small-scale test-setups to retain dynamic (and efficiency) similarity with the full-scale prototype, the Reynolds number (Re) should be high [43]. The Reynolds number for the reduced-scale tests are $\text{Re} = 6.8 \cdot 10^5 - 1.0 \cdot 10^6$ in turbine mode and $\text{Re} = 5.8 \cdot 10^5 - 1.0 \cdot 10^6$ in pump mode, indicating that the flow is fully turbulent and viscous effects are limited.

**Table 3**
Parameters and inertia constants for comparison of the full-scale system (prototype 1 in [6]) and the reduced-scale test-setup.

| Mechanical | Full-scale | | Reduced-scale (1:20.58) | |
|---|---|---|---|---|
| | Runner 1 | Runner 2 | Runner 1 | Runner 2 |
| $J$ [kg m$^2$] | $7.9 \cdot 10^4$ | $11.1 \cdot 10^4$ | 0.6[a] | 0.55[a] |
| $\omega_N$ [rad/s] | 6.4 | 6.4 | 141 | 141 |
| $\tau_N$ [N m] | $0.7 \cdot 10^6$ | $1.2 \cdot 10^6$ | 200 | 200 |
| $H_m$ [s] | 0.361 | 0.296 | 0.212 | 0.194 |
| Hydraulic | | | | |
| $L_c$ [m] | 60 | | 16 | |
| $A_c$ [m$^2$] | 78.5 | | 0.196 | |
| $Q_N$ [m$^3$/s] | 130 | | 0.380 | |
| $\Delta h_N$ [m] | 10 | | 7.8 | |
| $H_w$ [s] | 1.01 | | 0.41 | |

[a] Measured using a runout test as described in [44].

### 2.2. System characterization through experimental campaign

To characterize the full system, steady-state tests are performed in both turbine and pump mode for a range of speed ratios $\zeta = \omega_2/\omega_1$, where $\zeta = 0.752$ is the design ratio for both modes. In these tests,

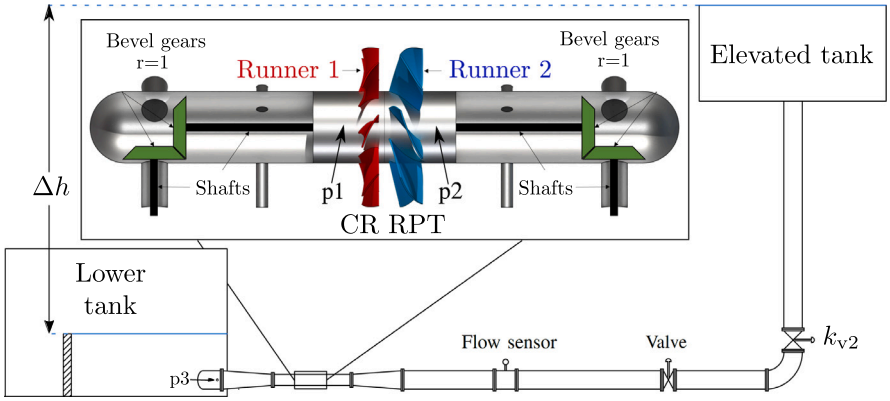


(a) Schematic overview of the experimental setup, with CR RPT location, mounting arrangement, and sensor locations.

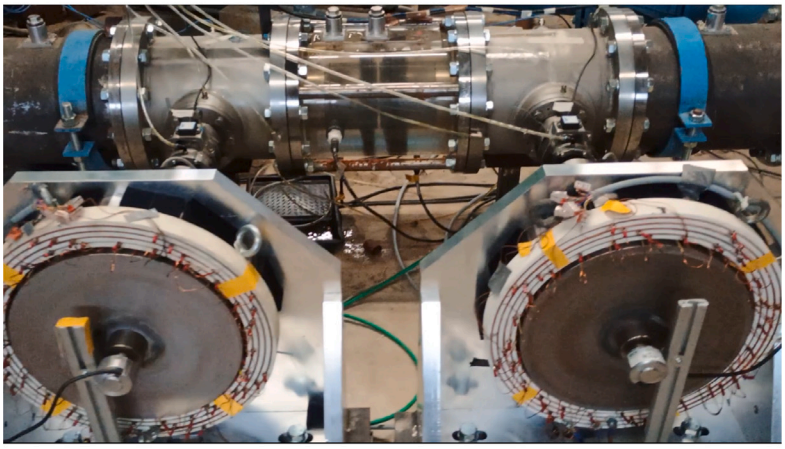

(b) The AF-PMSMs with the CR-RPT visible through the plexi-glass tube.

**Fig. 2.** Test-setup at Leichtweiß-Institute for Hydraulic Engineering and Water Resources of the TU Braunschweig [39].

the operating range limits of the rotational speed $\omega_1$ are defined by observation of cavitation in both modes, reverse flow in pump mode, and runaway conditions in turbine mode. Each operating point is run for 60 s and the steady-state results are averaged over 40 s.

### 2.2.1. RPT model

In Fig. 3, the measurement results for the CR RPT are shown, comprising the flow rate $Q$, the mechanical power $P$, the RPT efficiency $\eta_{RPT}$, and the machine torques $\tau_{m1,2}$ for varying rotational speeds $\omega_1$ and speed ratios $\zeta$. Here, the machine torques are calculated by adding (pump mode) or subtracting (turbine mode) the AF-PMSM friction torques $\tau_{f1,2}$ from the torque sensor measurements $\tau_{s1,2}$ in Eq. (3). These friction torques were previously characterized on a hardware-in-the-loop test-setup [44] with a linear model in Eq. (4), where $\alpha_1 = 1.26$ N m, $\alpha_2 = 1.04$ N m, $\beta_1 = 5.14 \cdot 10^{-3}$ N m s, and $\beta_2 = 5.96 \cdot 10^{-3}$ N m s. The mechanical power at the electric machines is calculated using Eq. (5). In Eq. (6), the RPT efficiency $\eta_{RPT}$ is calculated, where $h_{RPT}$ is determined using the pressure sensors $p_{1,2}$. Note that this efficiency also includes the mechanical efficiency of the PTO.

$$\tau_{m1,2} = \tau_{s1,2} \pm \tau_{f1,2}, \tag{3}$$

$$\text{where } \tau_{f1,2} = \alpha_{1,2} + \beta_{1,2} \cdot \omega_{1,2} \tag{4}$$

$$P = \tau_{m1}\ \omega_1 + \tau_{m2}\ \omega_2 \tag{5}$$

$$\eta_{RPT} = \frac{P}{g \cdot \rho \cdot Q \cdot h_{RPT}}\ \text{(Turbine)}, \tag{6}$$

$$\text{where } h_{RPT} = \frac{p_2 - p_1}{\rho \cdot g}$$

The low-speed limits in turbine mode and high-speed limits in pump mode are defined based on visual and acoustic assessment of cavitation development. In Fig. 3, the Thoma number is indicated for these operating range limits, which is an indicating measurement value for cavitating conditions. The Thoma number is defined as the net positive suction specific energy (at the pressure sensor $p_3$) divided by the RPT hydraulic specific energy [45]. It can be seen that in turbine mode, the lowest rotational speeds correspond to Thoma numbers of $\sigma = 1.96$ to $\sigma = 2.05$. In pump mode, the maximum rotational speeds correspond to Thoma numbers of $\sigma = 1.12$ to $\sigma = 1.20$, with an outlier for $\zeta = 1.0$, where $\sigma = 1.29$. Based on a study on cavitating flow conditions for the reduced-scale RPT [46], the measured Thoma numbers in turbine mode correspond to minimal cavitation inception on the leading edge of runner 1. In pump mode, the cavitation region encapsulates half the blade in runner 1, with limited cavitation inception occurring at the leading edge of runner 2 [46]. In Appendix A, the cavitation inception is pictured for four operating points. Apart from cavitation, the high-speed limits in turbine mode are defined based on the torque of runner 1 reaching 0, which would lead to unstable runaway conditions. For the low-speed limits in pump mode, low-frequency turbulence is assessed visually and acoustically, indicating flow separation and reverse flow.

The operating ranges are 52 rad/s $< \omega_1 <$ 131 rad/s in turbine mode and 99 rad/s $< \omega_1 <$ 141 rad/s in pump mode, where this range is highly influenced by the speed ratio $\zeta$ in pump mode. Contrary to the lower speed operating range, the power range in pump mode is larger, reaching from 24.6 kW to 47.3 kW compared with 9.5 kW$< P <$14.8 kW in turbine mode. The best efficiency point (BEP) in turbine mode is 85.0% at $\zeta = 0.8$, $\omega_1 = 83.8$ rad/s, and $P = 14.2$ kW. In pump mode, the

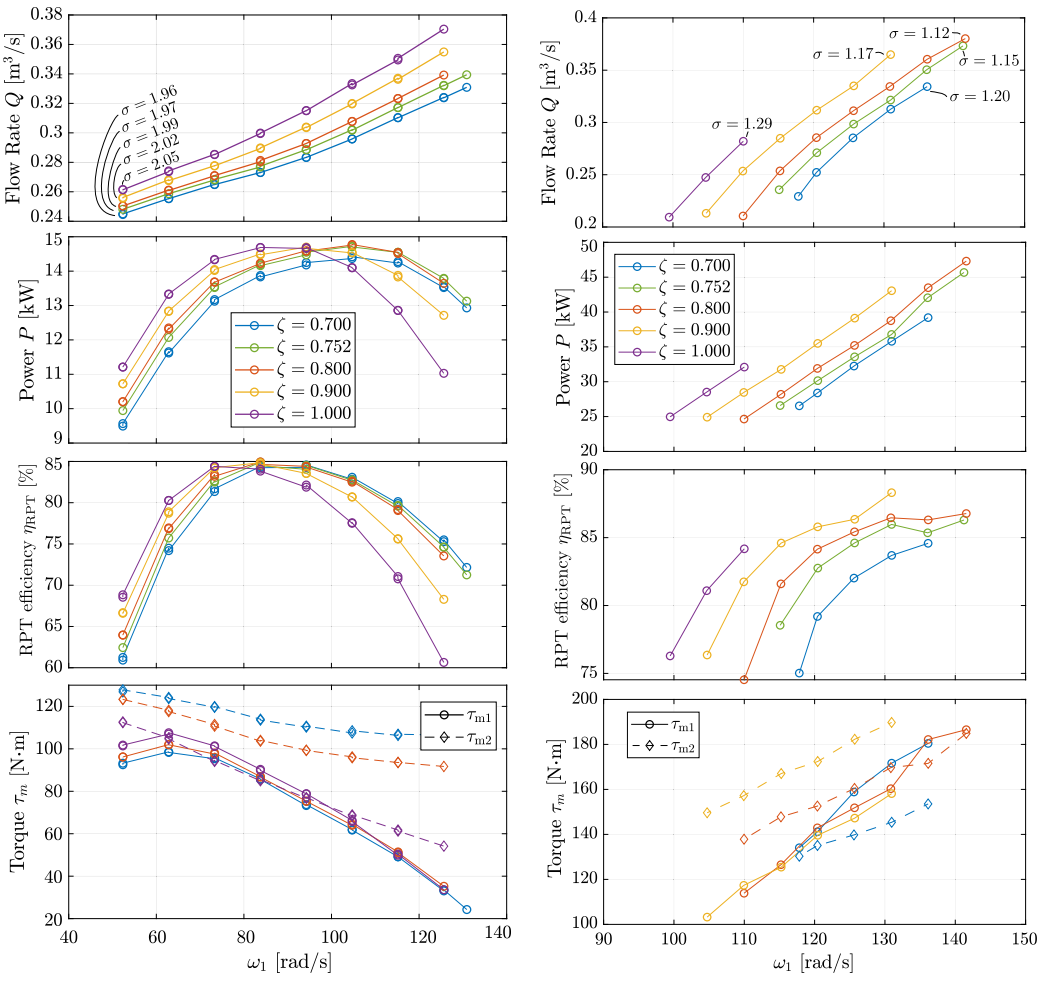


(a) Turbine mode. (b) Pump mode.

**Fig. 3.** Steady-state measurement results, comprising flow rate $Q$, mechanical power $P$, RPT efficiency $\eta_{\mathrm{RPT}}$, and machine torques $\tau_{\mathrm{m1,2}}$ versus rotational speed $\omega_1$ for different speed ratios $\zeta$, with Thoma numbers $\sigma$ indicated for the minimum speeds in turbine mode and maximum speeds in pump mode.

BEP is 88.3% at $\zeta = 0.9$, $\omega_1 = 130.9$ rad/s, and $P = 43.1$ kW. Note that the discrepancy in power between pump and turbine mode is high because of the relatively high conduit losses, which reach up to a head loss of 2 m in the experiments, compared to an expected maximum 0.5 m conduit loss in the full-scale system [47].

In turbine mode, the flow rate $Q$ increases with increasing rotational speed $\omega_1$ and speed ratio $\zeta$. Next, with increasing speed, the power $P$ also increases up to its maximum, after which the power starts to decrease due to a decrease in the RPT efficiency $\eta_{\mathrm{RPT}}$. At low speeds, the efficiency is the highest for speed ratio $\zeta = 1.0$, with the optimal speed ratio gradually decreasing for increasing rotational speed $\omega_1$ towards the BEP, after which the lowest speed ratio $\zeta = 0.7$ becomes optimal. Finally, the machine torques $\tau_{\mathrm{m1,2}}$ give an indication of the influence of the rotational speeds on the torque and power distribution between the two runners. Here, it is seen that for $\omega_1 > 63$ rad/s, the torque is inversely proportional to the rotational speed for both runners, which is also reflected in $\tau_{\mathrm{m2}}$ being higher for lower speed ratios $\zeta$. Inversely, for a certain rotational speed $\omega_1$ of the first runner, its torque $\tau_{\mathrm{m1}}$ increases with an increase in the speed ratio $\zeta$, which corresponds to an increase of the rotational speed of the upstream runner $\omega_2$. This highlights the hydraulic linkage between the two runners.

In pump mode, both the flow rate $Q$ and power $P$ increase with increasing $\omega_1$ and $\zeta$. However, contrary to turbine mode, the operating range is highly influenced by the chosen speed ratio. Especially for limit speed ratios $\zeta = 0.7$ and $\zeta = 1.0$, the operating range is significantly restricted. The RPT efficiency also increases with increasing $\omega_1$ and $\zeta$, with the exception of the high end speed range 130 rad/s $< \omega_1 <$ 141 rad/s for speed ratios $\zeta = 0.752$ and $\zeta = 0.800$, indicating the nonlinearity of the system. Looking at the machine torques $\tau_{\mathrm{m1,2}}$, it can be seen that $\tau_{\mathrm{m2}}$ increases with increasing speed ratio $\zeta$. Next, $\tau_{m1}$ is again significantly influenced by the speed of runner 2, which is downstream in pump mode, with $\tau_{m1}$ generally decreasing for an increasing speed ratio. Finally, for the high-end speed range with $\zeta = 0.8$, the nonlinearity of the hydraulic coupling is also highlighted. By increasing $\omega_1$ from 131 rad/s to 136 rad/s, the gradients of $\tau_{\mathrm{m1}}$ and $\tau_{\mathrm{m2}}$ respectively increase/decrease significantly, which is reversed when the speed is increased further to 141 rad/s.

Based on the measurement results, the RPT is characterized using three dimensionless coefficients that fully represent the system at variable fallhead and flow rate [47]. These coefficients are the head coefficient $C_h$ (Eq. (7)) and torque coefficients $C_{\tau 1,2}$ (Eq. (8)), which vary with the two tip speed ratios $\lambda_{1,2}$ (Eq. (9)) of the two runners.

$$C_{\mathrm{h}} = \frac{g\, h_{\mathrm{RPT}}}{\frac{1}{2}(Q/A)^2} \tag{7}$$

$$C_{\tau 1,2} = \frac{\tau_{\mathrm{m1,2}}}{\frac{1}{2}\,\rho\,Q^2/A\,R} \tag{8}$$

$$\lambda_{1,2} = \frac{R\,\omega_{1,2}}{Q/A} \tag{9}$$

Here, $R$ and $A$ are the runner radius (0.138 m) and runner area (0.0482 m$^2$), respectively. These coefficients are independent of flow

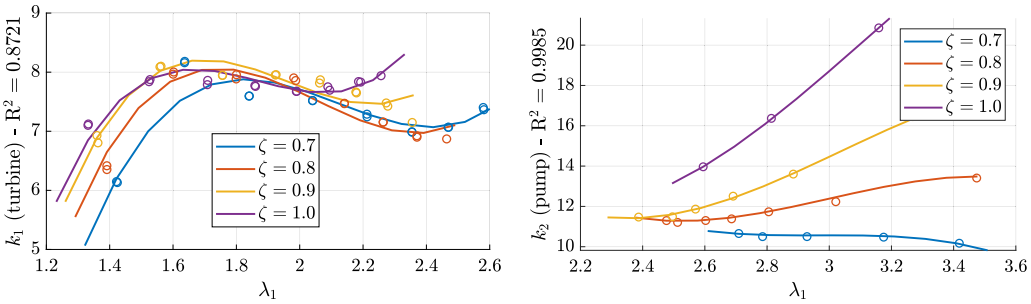


(a) Low-pressure side conduit loss coefficient $k_1$ in turbine mode.

(b) High-pressure side conduit loss coefficient $k_2$ in pump mode.

**Fig. 4.** Conduit loss coefficients $k$ for (a) the low-pressure side in turbine mode and (b) the high-pressure side in pump mode.

rate and rotational speeds, enabling to predict the performance at other fallheads. For each coefficient, a 3D third-degree polynomial regression model in both $\lambda_1$ and $\lambda_2$ is fit over the measurement results.

### 2.2.2. Conduit losses

Theoretically, the hydraulic losses of a unidirectional flow with constant Reynolds number can be described by the major (friction) and minor (local) losses, where the losses scale with the square of the flow rate $Q^2$. In Eq. (10), the major and minor losses are combined into one loss factor $k_1$ for the low-pressure side losses and $k_2$ for the high-pressure side losses, which allows to calculate the head loss $h_L$ for both sides.

$$h_{L,i} = k_i \frac{8}{\pi^2 D_i^4} \frac{Q^2}{g} \tag{10}$$

Experimentally, the head losses $h_{L,i}$ (and subsequently $k_i$) can be determined by comparing the total pressure at the reservoir surfaces to the total pressure at the RPT boundaries, as shown in Eq. (11). The head losses range from 1.24 m to 2.79 m in turbine mode and from 1.07 m to 3.23 m in pump mode.

$$h_{L,i} = \left| h_{s,i} - \frac{p_{i,\text{tot}}}{g \cdot \rho} \right|, \tag{11}$$

$$\text{where } p_{i,\text{tot}} = p_i + \frac{1}{2}\,\rho\,(Q/A)^2$$

From these experimental results, it is concluded that $k_i$ is not constant for all rotational speeds $\omega_1$ and speed ratios $\zeta$. The greatest variability in $k$ is observed at the outlet of the RPT ($k_1$ in turbine mode and $k_2$ in pump mode), due to the differences in, e.g., the Reynolds number and amount of flow separation caused by the RPT at different operating points. Therefore, $k_i$ is also characterized versus $\lambda_{1,2}$ with a third-degree polynomial fit, with the results for the downstream losses shown in Fig. 4. In turbine mode, loss coefficient $k_1$, representing the low-pressure side losses, is generally higher for high speed ratios and is minimal for low tip speed ratios. In pump mode, the discrepancy between the different speed ratios is apparent, with the high-pressure side losses significantly increasing with $\lambda_1$ for $\zeta = 1$, resulting in an almost twofold increase compared with the average loss coefficient $k_2$. In contrast, for $\zeta = 0.7$, the loss coefficient decreases with increasing $\lambda_1$, illustrating the influence of the CR RPT rotational speeds on the flow uniformity.

### 2.2.3. Power-efficiency dataset

Using the characterization coefficients of both the RPT and the conduit, a numerical dataset $\boldsymbol{\mathcal{D}}$ is calculated. The dataset $\boldsymbol{\mathcal{D}}$ relates two input variables, i.e., the two variable DOFs $\omega_1$ and $\omega_2$ to the two output parameters, the mechanical power $P$ at the AF-PMSMs and the total efficiency $\eta$.

$$\boldsymbol{\mathcal{D}}(\omega_1, \omega_2) = [P, \eta] \tag{12}$$

The dataset $\boldsymbol{\mathcal{D}}$ is populated by numerically varying the inputs over the following intervals in turbine and pump mode, respectively:

$$\omega_1 \text{ (rad/s)} \in [52 : 1 : 131] \;/\; \omega_1 \in [-99 : -1 : -141] \tag{13}$$

$$\omega_2 \text{ (rad/s)} \in [37 : 1 : 131] \;/\; \omega_2 \in [-82 : -1 : -120] \tag{14}$$

Here, the standard MATLAB® array notation is used, including the data increments for each variable, which determine the resulting resolution of the dataset $\boldsymbol{\mathcal{D}}$.

For each combination of input variables, the flow rate $Q$ is calculated by solving the law of conservation of energy for a steady and incompressible flow:

$$h_{RPT}(Q) + \text{sign}(Q) \cdot h_L(Q) = \Delta h \tag{15}$$

In Eq. (15), $h_{RPT}$ is the RPT head (Eq. (7)) and $h_L$ are the conduit losses (Eq. (10)). This equation is numerically solved for the full range of $\omega_1$, $\omega_2$, using the characterization surfaces for $C_h$, $k_1$ and $k_2$. Finally, the mechanical power $P$ is calculated using the characterization surfaces for $C_{\tau 1,2}$ in Eq. (16). The total efficiency in turbine mode is determined using Eq. (17).

$$P = \sum_{i=1}^{2} \frac{1}{2}\,\rho\,\frac{Q^2}{A}\,R \cdot C_{\tau_i} \cdot \omega_i \tag{16}$$

$$\eta = \frac{P}{\rho\, g\, Q\, \Delta h} \quad \text{(Turbine)} \tag{17}$$

## 3. Methodology

### 3.1. Control architecture

To provide frequency control with the CR RPT, the authors developed a lookup table-based control architecture that dynamically changes the system power $P$. The control aims to optimize two key performance indicators: the total efficiency $\eta$ and the power rise time $T_r$. Furthermore, the power response is shaped through adaptive torque limitations on both runners, which scale based on the modeled power distribution between the two runners and the measured rotational speeds. A schematic overview of the control architecture is outlined in Fig. 5. A distinction is made between the high-level control, where the optimal rotational speed setpoints are selected, and the low-level control, where the speed setpoints are converted into torque setpoints.

### 3.1.1. High-level control

Based on the characterization tests, described in Section 2.2, a lookup table $\boldsymbol{\mathcal{L}}$ is numerically populated through 2D interpolation of the dataset $\boldsymbol{\mathcal{D}}$ over the possible power setpoints with a resolution of 0.1 kW. The matrix $\boldsymbol{\mathcal{L}}$ stores all possible combinations of the speed setpoints $\hat{\omega}_{1,2}$, together with their characterized efficiency $\eta^*$, steady-state torque setpoints $\tau^*_{m1,2}$ and power distribution $P^*_{1,2}$ for a range of possible power setpoints $\hat{P}$.

$$\boldsymbol{\mathcal{L}}(\hat{P}) = [\hat{\boldsymbol{\omega}}_1, \hat{\boldsymbol{\omega}}_2, \boldsymbol{\eta}^*, \boldsymbol{\tau}^*_{m1}, \boldsymbol{\tau}^*_{m2}, \boldsymbol{P}^*_1, \boldsymbol{P}^*_2] \tag{18}$$

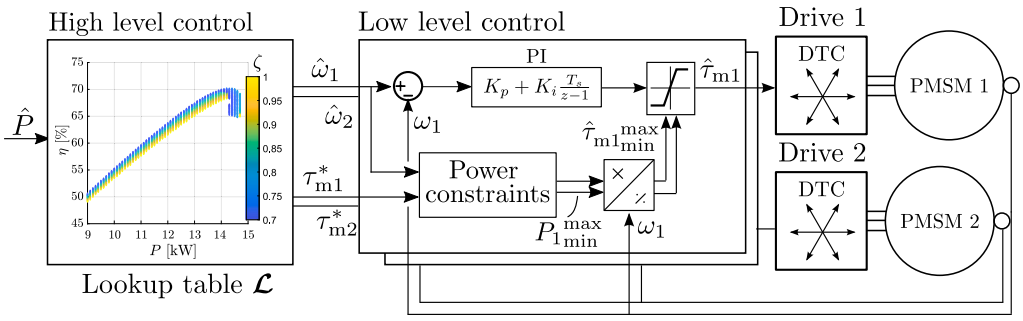


**Fig. 5.** Schematic overview of the control architecture.

It is important to note that the direct torque control in ABB drives causes a small steady-state error between the torque setpoints $\hat{\tau}_{m1,2}$ and the actual (measured) machine torques $\tau_{m1,2}$, as outlined in Appendix B. Therefore, lookup table $\mathcal{L}$ is populated with the expected steady-state torque setpoints $\tau^*_{m1,2}$ and power distribution $P^*_{1,2}$, instead of the actual measured torques $\tau_{m1,2}$ and powers $P_{1,2}$ during the characterization tests. However, for the validation, the measured power response is still used. Fig. 6 visualizes the lookup table $\mathcal{L}$, where the efficiency is plotted over the range of $\hat{P}$ for the different possible speed ratios $\zeta$. Furthermore, for every power setpoint $\hat{P}$, the RPT efficiency $\eta_{RPT}$ and rotational speed combination $\omega_{1,2}$ are also shown. Note that the total efficiency is significantly lower than the RPT efficiency due to the inclusion of the conduit losses. In turbine mode, the efficiency is minimal for the lowest power of 9 kW, with a total efficiency of 50.6%. The efficiency increases to a maximum of 70.2% at $\hat{P} = 14.3$ kW, after which the efficiency decreases up to the maximum power of 14.7 kW. For all power setpoints < 13.5 kW, speed ratio $\zeta = 0.7$ has the highest total efficiency, with $\zeta = 1.0$ having an efficiency deficit of 1.4% at 9 kW up to 2.1% at 13.5 kW in comparison. The optimal $\omega_1$ in this power region ranges from 49.8 rad/s to 76.8 rad/s. Interestingly, the optimal speed ratio for the RPT efficiency in this region is $\zeta = 1.0$, as shown in Fig. A.13(c). However, because a higher flow rate induces more conduit losses, the total efficiency decreases for this speed ratio. For powers higher than 13.5 kW, the optimal speed ratio gradually increases to $\zeta = 0.82$.

In pump mode, shown in Fig. 6(b), the maximum total efficiency is 68.9% at a power of 29.5 kW and a speed ratio of $\zeta = 0.78$. This efficiency decreases to 66.3% at $\hat{P} = 25$ kW ($\zeta = 0.83$) and to 62.8% at $\hat{P} = 45$ kW. Contrary to turbine mode, the optimal speed ratio significantly varies in pump mode, with $\zeta = 0.83$ at $\hat{P} = 45$ decreasing to $\zeta = 0.78$ at the maximal efficiency point, after which $\zeta$ increases to > 0.90 for $\hat{P} > 38.1$ kW. Finally, for $\hat{P} > 43.0$ kW, the speed ratio decreases towards $\zeta = 0.78$ for the highest power setpoints.

For a given power setpoint $\hat{P}$, the operating point with the highest efficiency is selected, which corresponds to a reduction of $\mathcal{L}$ to a 1D array. With this approach, the overall efficiency is maximized. Furthermore, it allows to perform an iterative optimization of the reduced lookup table by performing an additional offline test over the power operating range to update the actual measured powers in $\mathcal{L}$ and minimize the steady-state error of the power response.

#### 3.1.2. Low-level control

The low-level control converts the speed setpoints $\hat{\omega}_{1,2}$ to respective torque setpoints $\hat{\tau}_{m1,2}$. These torque setpoints are sent to the ABB drives, which use an internal direct torque controller (DTC) to define the output voltage vectors [48]. The torque setpoints are determined using PI-controllers with clamping anti-windup. Furthermore, in order to shape the power response, an adaptive torque limitation is added for each runner individually. In this novel approach, $P_{i,min}{}^{max}$ are the power limits for runner $i$, with the power limits for both runners adding up to the total power limit $P_{tot,min}{}^{max}$. The torque-setpoint limits are found by dividing the runner power limit by the current rotational speed, ensuring that the power limit is not exceeded in Eq. (19).

$$\hat{\tau}_{mi,min}{}^{max} = \frac{P_{i,min}{}^{max}}{\omega_i(k)} \tag{19}$$

Although the distribution of the total power limit is application-specific, it is aided by the power distribution stored in the lookup table $P^*_i(P_{tot,min}{}^{max}) \in \mathcal{L}(P_{tot,min}{}^{max})$. The specific implementation for FCR operation is outlined in the following section.

### 3.2. Frequency containment reserve (FCR)

To validate the dynamic behavior of the developed control architecture, it is investigated whether the system is able to provide FCR. In FCR, the power setpoint is updated at a frequency of 1 Hz, based on deviations in the grid frequency. During FCR, the system is running at a base power of $P_b$ and an FCR capacity $P_{FCR}$ is allocated. The exact regulations for FCR depend on the region. Here, the regulations for Continental Europe are used, as described in European Regulation 2017/1485 [4]. If the frequency deviation $\Delta f = f(t) - 50$ Hz is within the deadband of ±10 mHz, the system keeps operating at the base power $P_b$. In case of a larger frequency deviation, the delivered balancing reserve scales linearly with the frequency deviation as outlined in Eq. (20), where the ± sign represents + in pump mode and − in turbine mode. When the frequency deviation $\Delta f$ exceeds ±200 mHz, the full capacity of $P_b(t) \pm P_{FCR}$ is activated. Full reserve activation must be delivered without artificial delay and within 30 s. Furthermore, at least 50% is to be delivered after 15 s, with the power response at least linear from 15 s to 30 s. These regulations are currently active in Austria, Belgium, Denmark, France, Germany, the Netherlands, and Switzerland.

$$\hat{P}(t) = P_b \pm \frac{f(t) - 50\ \text{Hz}}{190\ \text{mHz}} \cdot P_{FCR} \tag{20}$$

In addition to these minimum requirements, transmission system operators provide additional requirements for the power response shape. Fig. 7 shows the main requirements for Frequency Containment Reserve (FCR) since June 2022 in Germany [49]. These requirements concern the allowed and tolerable fluctuations on the power response during a pre-qualification test. In this test, a step response with full FCR capacity $P_{FCR}$ is performed, and the response time and power fluctuations are analyzed. Two ranges are defined: The 'allowed' range, in which > 95% of the measured power response must lie and the 'tolerable' range, in which < 5% of the values may lie. The power response is split into three phases: the initial stationary period (SP), the power change period (PCP), and the transient period (TP). The TP ends 90 s after the power setpoint change, reverting back to the SP. All three phases have different range limits denoted as a percentage of $P_{FCR}$ [49], as outlined in Fig. 7. In this study, power limits are implemented to comply with the requirements for FCR, with Eq. (21) implemented after a power setpoint change, and Eq. (22) after the setpoint is reached:

$$P_{i,min}{}^{max} = P^*_i\left[{}^{max}_{min}\left(\hat{P}(k_0 - 1), \hat{P}(k_0)\right)\right] \pm 10\% \cdot P_{FCR} \tag{21}$$

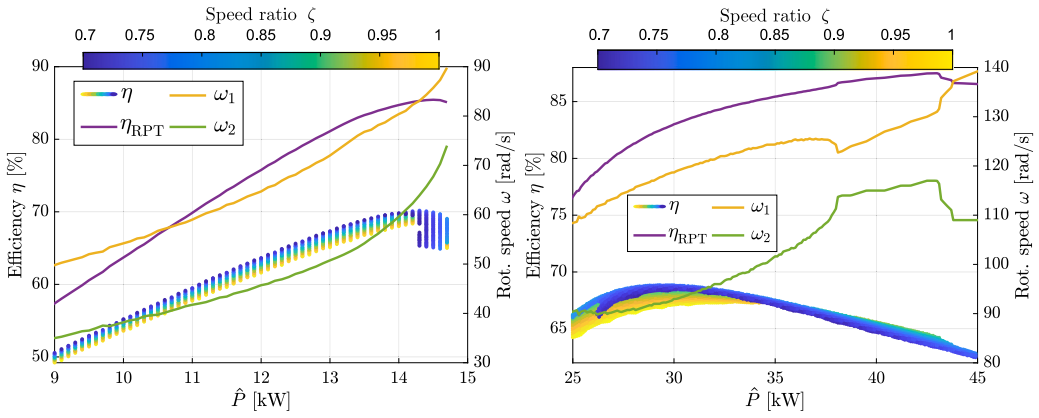


**Fig. 6.** Representation of lookup table $\mathcal{L}$ in (a) turbine mode and (b) pump mode, with the total efficiency $\eta$ plotted for all possible operating points, and $\eta_{RPT}$ and $\omega_{1,2}$ plotted for the operating point with the optimal total efficiency for a certain power setpoint $\hat{P}$.

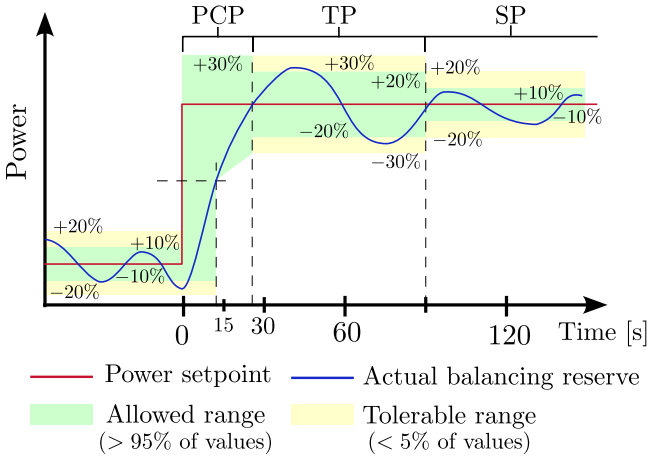


**Fig. 7.** Allowed and tolerable fluctuations during FCR operation [49].

$$P_{\mathrm{i,min}}^{\mathrm{max}} = P_i^* \left[\hat{P}(k_0)\right] \pm 10\% \cdot P_{\mathrm{FCR}} \tag{22}$$

Here, $P_{\mathrm{FCR}}$ is the reserve capacity and $k_0$ is the sample at which the power setpoint $\hat{P}$ changes, with $\hat{P}(k_0 - 1)$ being the previous power setpoint.

In Section 4.1, a pre-qualification test is performed, i.e., the power response of the CR RPT at full FCR capacity is analyzed, and it is validated that the control architecture meets the imposed requirements to perform FCR. Finally, the control is validated on multiple 10 min frequency patterns in Section 4.2. Here, three historic frequency measurements from the Continental Europe synchronous area are used as archived by Netztransparenz [50]. To avoid seasonal influences, a dataset is selected from the months June 2023, October 2023, and February 2024. From these months, the 10 min intervals with the largest deviations in frequency are selected to validate the control. As illustrated in Fig. 8, the frequency fluctuations are limited, with a maximum 10 minute difference of 0.213 Hz, and a maximum 1 second jump of 0.031 Hz, both found from the June 2023 dataset. Therefore, in order to validate that the developed control architecture also works for future, more volatile frequency patterns, a random frequency pattern is generated with values between 49.80 Hz $< f <$ 50.20 Hz, where the maximum 1 second jump is limited to 0.05 Hz.

## 4. Results

In this section, the full reserve capacity power response of the CR RPT is analyzed in Section 4.1. Furthermore, an FCR use case is performed in Section 4.2, followed by a discussion of the results in Section 4.3. The PI-controllers and weighting factors were tuned in a hardware-in-the-loop test-setup, described in [44]. The PI controllers were tuned by optimally shaping the step response in terms of rise time, settling time and overshoot of the speed setpoints, which resulted in a bandwidth of > 1 Hz, and a gain and phase margin of respectively > 10 dB and > 45° over the operating range. The proportional and integral factors are respectively $K_p$ = 7.0 N m s and $K_i$ = 5.0 N m for runner 1, and $K_p$ = 7.4 N m s and $K_i$ = 10.0 N m for runner 2. The power response $P$ is again calculated using Eq. (5), including the AF-PMSM friction. However, in these dynamic tests, the measured machine torques $\tau_{\mathrm{m1,2}}$ also take into account the acceleration/deceleration torque of the AF-PMSMs.

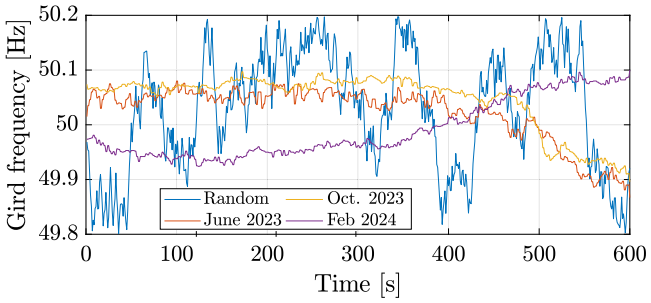


**Fig. 8.** Historic frequency data from June 2023, October 2023, and February 2024 [50], and a random frequency pattern.

$$\tau_{\mathrm{m1,2}} = \tau_{\mathrm{s1,2}} \pm \left(\tau_{\mathrm{f1,2}} + J \cdot \frac{\Delta\omega_{1,2}}{t_s}\right), \tag{23}$$

where $J$ = 0.53 kg m$^2$ is the rotational inertia of the AF-PMSMs [44] and $t_s$ is the sample time. During the characterization tests, a significant fluctuation was observed on both the speed and torque measurements, with frequencies $f = N \cdot \omega/(2 \cdot \pi)$ [Hz], where $N \in \mathbb{N}$, indicating a stress cycle at each rotation, with multiples also present in the frequency spectrum. These fluctuations typically originate from imperfect alignment in the mechanics [51]. In the following results, these frequencies are specifically filtered out using multiple variable-frequency bandstop filters with a bandwidth of 4 Hz. Furthermore, high-frequency noise is filtered out using a 50 Hz lowpass filter.

### 4.1. Full reserve power step response

#### 4.1.1. Turbine mode

The power response of full reserve activation (both upward and downward) with $P_b$ = 11.5 kW and $P_{\mathrm{FCR}}$ = 2.5 kW is shown in

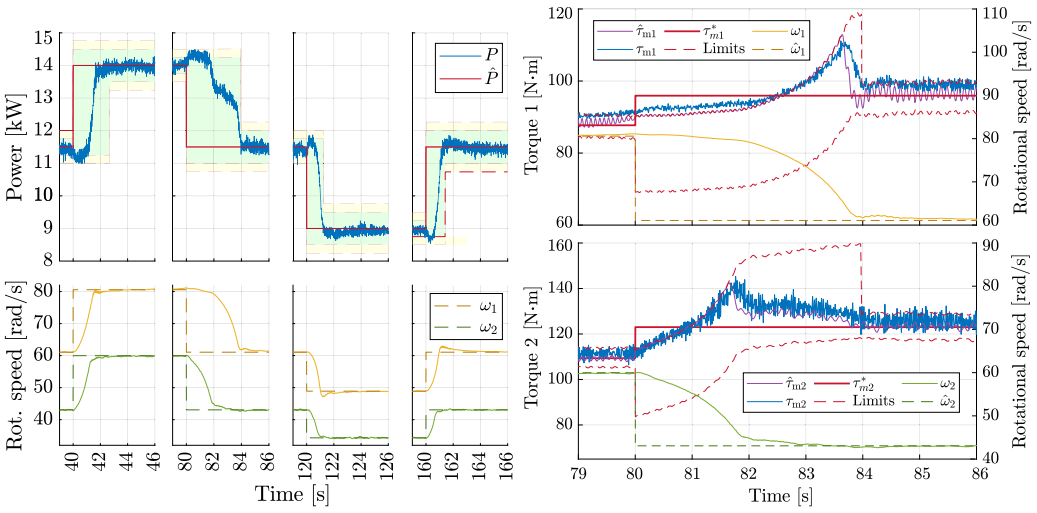


(a) Step response of full reserve activation in turbine mode with $P_b = 11.5$ kW and $P_{\text{FCR}} = 2.5$ kW.

(b) Torque and speed response for both runners for the second step in (a).

**Fig. 9.** Full reserve activation results in turbine mode.

Fig. 9(a). Here, the limits for the allowed and tolerable ranges are indicated. Within the high-efficiency region in turbine mode, power and rotational speed are proportionate (see Fig. 6(a)). Therefore, an increase in the power setpoint corresponds to an increase in the rotational speed. However, to allow the fluid to accelerate the runners, the low-level PI controllers decrease the machine torques. Therefore, the machine power momentarily dips before increasing, indicating non-minimum phase system behavior. For a power decrease, the behavior is identical but opposite. Without the novel torque constraints, outlined in Section 3.1.2, this initial inverse response to the setpoint exceeds the power constraints imposed to provide frequency control. Fig. 9(a) shows that, using the adaptive torque limits, the power response $P$ mostly stays well within the allowed region, with the exception of the initial response, where the power exceeds the ±10% allowed range, but does not exceed the tolerable ±20% range.

The power rise times $T_r$ during the PCP and relative root mean square deviations (RMSD) during the TP and SP are listed in Table 4. Here, the rise time is defined from 0% to 100% of the step. The relative RMSD $\epsilon_p$ is defined as the root mean square deviation of the measured power divided by 10% of the reserve capacity:

$$\epsilon_p(P) = \frac{\sqrt{\frac{1}{n}\sum_{i=1}^{n}\left(P_i - \hat{P}_i\right)^2}}{10\% \cdot P_{\text{FCR}}} \tag{24}$$

Here, $10\% \cdot P_{\text{FCR}} = 250$ W in turbine mode. The rise times are considerably faster than the 30 s limit imposed when providing FCR. The rise times for steps 1 and 2 (11.5 kW ↔ 14 kW) are considerably longer than for steps 3 and 4 (11.5 kW ↔ 9 kW), as the magnitude of the rotational speed steps is almost double in the first case. The relative RMSDs for the four steps (during TP and SP) are between 48% to 58%, which is well within the allowed ±10% (250 W) interval. Step 2, having the longest rise time, is highlighted in Fig. 9(b). Here, the torque and speed response of runner 1 and runner 2 are shown. Note that in these graphs, contrary to the power graphs, the limits are applied to the torque setpoints $\hat{\tau}_{\text{m1,2}}$, instead of the measured torques $\tau_{\text{m1,2}}$, as explained in Appendix B. In this downward power step, the speed setpoints are reduced for both runners. Simultaneously, the minimum torque limit is reduced according to the decrease in power setpoint. However, to avoid exceeding the tolerable power range, the maximum power limit (and thus torque limits $\hat{\tau}_{\text{mi,max}}$) remains unchanged. In order to decrease the rotational speeds, the torque setpoints $\hat{\tau}_{\text{m1,2}}$ increase to the maximum limit. As the power limits remain constant in the PCP, the torque limits evolve with the rotational speeds during the deceleration, allowing for higher torque to further increase the deceleration. At $t = 83.92$ s, the PCP ends, which tightens the maximum power (and torque) limits.

**Table 4**
Power response rise times $T_r$ and relative root mean square deviations $\epsilon_p$ during TP and SP for full reserve activation.

| Step nr. | Turbine | | Pump | |
|---|---|---|---|---|
| | $T_r$ | $\epsilon_p$ | $T_r$ | $\epsilon_p$ |
| 1 | 2.57 s | 48% | 0.18 s | 39% |
| 2 | 3.92 s | 51% | 0.19 s | 26% |
| 3 | 1.29 s | 41% | 0.23 s | 16% |
| 4 | 1.51 s | 58% | 0.23 s | 38% |

#### 4.1.2. Pump mode

In pump mode, the full reserve activation with $P_b = 35$ kW and $P_{\text{FCR}} = 10$ kW is shown in Fig. 10. In contrast to turbine mode, at an increase in power and speed in pump mode, the PI controllers also increase the machine torques to accelerate the runners, averting the initial dip in the power response. This is reflected in the rise times, which are only 0.18 s to 0.23 s. Furthermore, the power response $P$ always remains well within the allowed region, even during the initial response. The relative RMSDs for the four steps are between 16% to 39% relative to the $\pm 10\% \cdot P_{\text{FCR}} = \pm 1000$ W allowed region. Note that, in pump mode, the power setpoint is always reached before the speed setpoints are reached. Therefore, the torque limits are tightened when both rotational speeds have reached their setpoint. Note that the power limits in Fig. 10 remain as outlined by the FCR requirements, and the power response remains within the allowed (green) region. In Fig. 10(b), step 2, going from 45 kW → 35 kW, is highlighted. In this downward power step, the speed setpoints are reduced for both runners. Simultaneously, the minimum torque limit is decreased, according to the decrease in power setpoint, with the maximum torque limit unchanged. In order to decrease the rotational speed, the torque setpoints $\hat{\tau}_{\text{m}}$ decrease to the minimum limit. At $t = 82.81$ s, the torque limits are tightened.

### 4.2. FCR scenario

#### 4.2.1. Turbine mode

In Fig. 11, FCR is performed with $P_b = 11.5$ kW and $P_{\text{FCR}} = 2.5$ kW for the random frequency pattern (see Fig. 8). It is shown that the control manages to track the fast-changing power setpoint. During the 10-minute test, an overall relative RMSD of $\epsilon_p = 149\%$ relative to the $10\% \cdot P_{\text{FCR}}$ is found, as listed in Table 5. Note that in this FCR case, the $10\% \cdot P_{\text{FCR}}$ value is not a limit, but only gives an indication on the

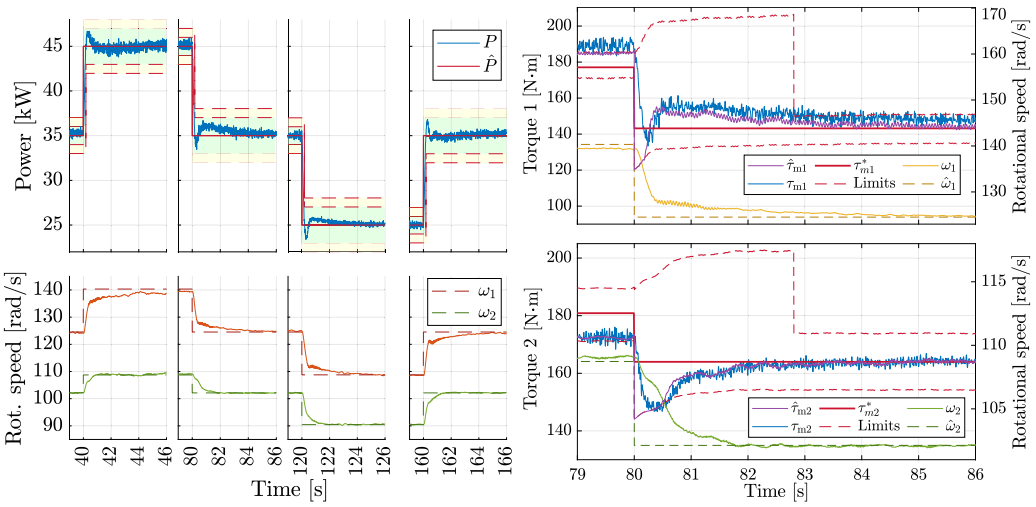


(a) Step response of full reserve activation in pump mode with $P_b = 35$ kW and $P_{\text{FCR}} = 10$ kW.

(b) Torque and speed response for both runners for the second step in (a).

**Fig. 10.** Full reserve activation results in pump mode.

**Table 5**
Measurement results for an FCR case with a random frequency set, where $\overline{\eta}$ and $\overline{\eta}_{\text{RPT}}$ are the average total and RPT efficiency, respectively.

| | Random | | June 2023 | | Oct. 2023 | | Feb. 2024 | |
|---|---|---|---|---|---|---|---|---|
| | Turbine | Pump | Turbine | Pump | Turbine | Pump | Turbine | Pump |
| $\epsilon_p(P)$ | 149% | 55% | 64% | 42% | 53% | 37% | 60% | 37% |
| $\epsilon_\omega(\omega_1)$ | 1.7% | 1.0% | 0.4% | 0.4% | 0.3% | 0.3% | 0.2% | 0.6% |
| $\epsilon_\omega(\omega_2)$ | 1.7% | 1.5% | 0.5% | 0.7% | 0.3% | 0.3% | 0.3% | 0.7% |
| $\overline{\eta}$ | 57% | 66% | 58% | 66% | 57% | 66% | 60% | 67% |
| $\overline{\eta}_{\text{RPT}}$ | 75% | 80% | 77% | 81% | 75% | 81% | 79% | 80% |

dynamics. However, it is seen in Section 4.1 that relative RMSD values up to $\epsilon_p = 58\%$ are also present in steady state. Therefore, the relative RMSDs of the rotational speeds are also listed, as they are negligible in steady state. Importantly, contrary to those of power, the relative RMSDs of rotational speeds ($\epsilon_\omega$) are calculated relative to the average of the setpoints:

$$\epsilon_\omega(\omega) = \frac{\sqrt{\frac{1}{n}\sum_{i=1}^{n}\left(\omega_i - \hat{\omega}_i\right)^2}}{\frac{1}{n}\sum_{i=1}^{n}\hat{\omega}_i} \tag{25}$$

In the random frequency case, $\epsilon_\omega(\omega_1) = \epsilon_\omega(\omega_2) = 1.7\%$. Finally, the flow rate $Q$, total efficiency $\eta$, and RPT efficiency $\eta_{\text{RPT}}$ are also plotted in Fig. 11, with average efficiencies of $\overline{\eta} = 57.3\%$ and $\overline{\eta}_{\text{RPT}} = 75.2\%$. In addition to the random frequency pattern, the results for the historic frequency datasets are also listed in Table 5. Here, it is shown that the power response is able to follow the historic frequency fluctuations more closely, through a significant reduction in the RMSDs of the power (53% to 64%) and rotational speeds (0.2% to 0.5%). Note that June 2023 has the highest variability in the frequency (see Fig. 8) and correspondingly has the highest RMSD values among the historic frequency datasets.

#### 4.2.2. Pump mode

The results for the FCR case in pump mode for the random frequency dataset are outlined in Fig. 12, with $P_b = 35$ kW and $P_{\text{FCR}} = 10$ kW. The control also manages to accurately track the power setpoint in this mode, with a relative RMSD of the power response of $\epsilon_p = 55\%$. The relative RMSDs of the rotational speeds are 1.0% and 1.5%, respectively. Finally, the efficiencies in pump mode fluctuate less than in turbine mode, with average values of $\overline{\eta} = 66.0\%$ and $\overline{\eta}_{\text{RPT}} = 79.9\%$. Similarly to turbine mode, the less volatile historic frequency datasets cause the power setpoint to be followed more closely, with relative RMSD values of the power between 37% and 42%. The RMSD values for the rotational speeds of runner 1 and runner 2 are reduced to 0.3%–0.7%.

### 4.3. Discussion

The results of this study demonstrate the effectiveness of the proposed dual variable-speed control architecture in dynamically shaping the power response of a contra-rotating pump–turbine for frequency containment reserve (FCR) applications. The rise times for full reserve activation are $< 3.92$ s and $< 0.23$ s in turbine and pump mode, respectively. When scaled to the full-scale 10 MW system with a factor of 1.53 to 2.46 based on the inertia constants, these rise times would become $< 9.64$ s and $< 0.57$ s, which is still significantly lower than the $< 30$ s limit imposed in Europe. Furthermore, it is found that the power response stays well within the allowed range, with the only exception being the initial dip/peak at a respective power setpoint increase/decrease in turbine mode, which stays within the tolerable range. After the power setpoint is reached, the power response has an RMSD of $< 58\%$ in turbine mode and $< 39\%$ in pump mode, relative to the allowed range. Further validation based on both historic frequency measurements and a highly volatile frequency patterns confirms that the control architecture can accurately perform FCR, in which the power setpoint is updated at 1 Hz. For the latter, most volatile frequency pattern, relative RMSD values for the rotational speeds are 1.7% for both runners in turbine mode, and 1.0% and 1.5% in pump mode for the respective runners, indicating precise control.

Contrary to direct power PID control through the runner torques (see Table 1), this model-based control ensures optimal efficiency at different power setpoints. Furthermore, it allows for large power steps and does not require a large turbine inertia. Unlike iterative search algorithms and existing lookup table-based control, the power response is fast, while power fluctuations are limited through adaptive torque constraints. Finally, although MPC also allows to optimally shape the power response, the proposed methodology does not require a dynamic model of the RPT and has a low computational cost. The proposed power shaping methodology can also be applied to traditional pump–turbines to increase their share in grid services.

## 5. Conclusions

This study presents a novel control architecture for a CR RPT to enhance the performance of low-head PHS systems in grid frequency

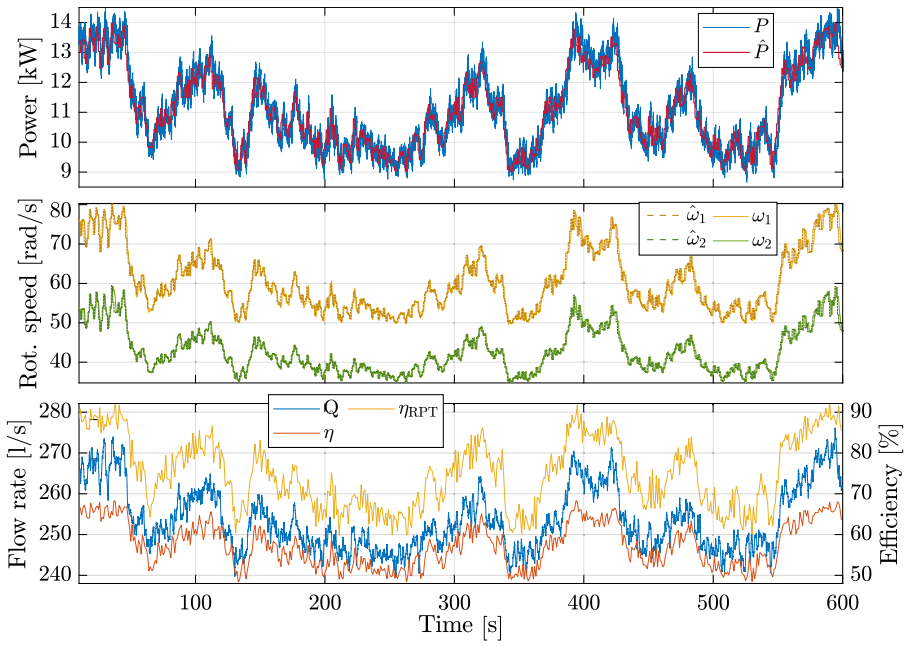


**Fig. 11.** Frequency containment reserve case with a random frequency pattern in turbine mode.

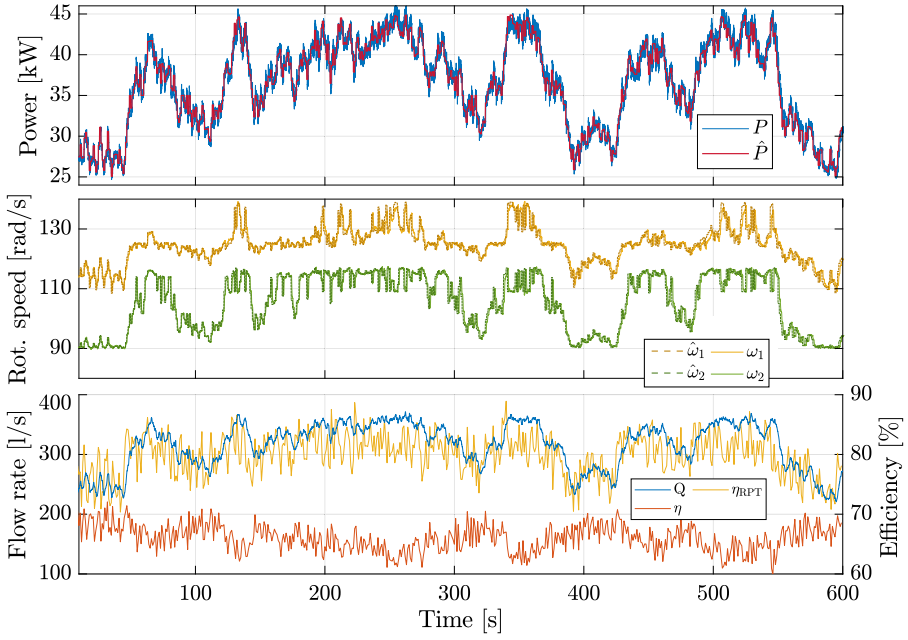


**Fig. 12.** Frequency containment reserve case with a random frequency pattern in pump mode.

control. The proposed dual variable-speed control optimizes the efficiency while dynamically shaping the power response to minimize the rise time and constrain power fluctuations. The power shaping is achieved through the runner torques, leveraging the modeled power distribution between the two runners and real-time rotational speed feedback. The torque constraints can be tuned to meet various frequency control requirements and local regulations. Experimental tests on a 45 kW reduced-scale (1:20.58) CR RPT show that dual variable-speed operation allows to increase both the operating range and the efficiency over that operating range, with maximum efficiencies of 85.0% in turbine mode and 88.3% in pump mode.

The validation of the developed control architecture shows that the full reserve activation rise times are $< 3.92$ s and $< 0.23$ s in turbine and pump mode, respectively. When scaled to a full-scale 10 MW system, the rise times are still significantly below the $< 30$ s allowed limit to perform FCR in Europe. Furthermore, the power response remains well within the allowed limits, with deviations within the tolerable range occurring only during the initial power setpoint response in turbine mode. Further validation using both historical and highly fluctuating frequency patterns confirms that the control architecture can accurately perform FCR. For the most volatile frequency pattern, the relative rotational speed RMSD is 1.7% and $\leq 1.5\%$ in turbine and pump mode, respectively, indicating precise tracking of the dynamic power setpoint.

These findings demonstrate that the proposed control methodology manages to track a dynamically varying power setpoint at optimal efficiency within imposed power constraints with a dual variable-speed CR RPT. This enables low-head PHS systems to provide frequency control services, such as FCR. Therefore, the implementation of these

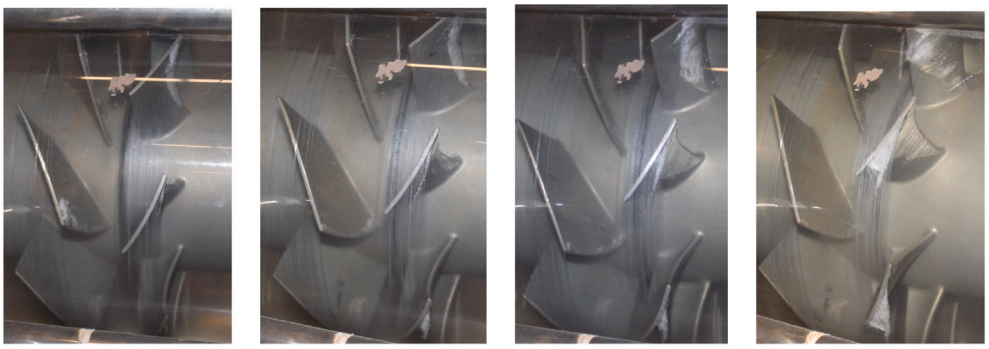

(a) OP1 $\sigma = 1.46$. (b) OP2 $\sigma = 1.39$. (c) OP3 $\sigma = 1.32$ (d) OP4 $\sigma = 1.20$.

**Fig. A.13.** Pictures of the RPT in pump mode with visible cavitation inception for four operating points.

**Table A.6**
Operating point (OP) measurement values for the illustration of cavitation inception.

| | $\omega_1$ [rad/s] | $\omega_2$ [rad/s] | $\sigma$ [–] | $h_{RPT}$ [m] |
|---|---|---|---|---|
| OP1 | 107 | 90 | 1.46 | 8.5 |
| OP2 | 119 | 93 | 1.39 | 8.9 |
| OP3 | 124 | 101 | 1.32 | 9.4 |
| OP4 | 139 | 109 | 1.20 | 10.2 |

low-head PHS systems can allow to increase the share of intermittent renewable energy sources. As these systems can be installed in rivers and shallow seas, they can complement the existing high-head PHS and electrochemical battery systems in order to further the energy transition. Finally, the proposed power shaping methodology can also be applied to traditional pump–turbines to further their grid services.

As potential avenues for future research, the authors foresee three key aspects. First, participation in frequency reserves leads to increased wear and fatigue in the RPT and the conduit. Although multiple studies have described this effect for high head systems [52,53], the dynamic loads of a low-head CR RPT can differ significantly because of the relatively high flow rate and runner interaction. These findings can allow the identification of critical components, which can be modeled and monitored for predictive maintenance [54]. Second, an economic analysis on the balance between the revenue of frequency reserves and the increased cost of maintenance can provide insights into the optimal operation of the system. Finally, the authors plan to develop a model predictive controller for the CR-RPT to investigate whether the variable-speed ratio between the two runners can be further exploited to shorten the rise time in turbine mode. The measurement data acquired in this study can be used to create a dynamic model of the RPT.

## CRediT authorship contribution statement

**Daan P.K. Truijen:** Writing – review & editing, Writing – original draft, Visualization, Validation, Software, Methodology, Investigation, Formal analysis, Data curation, Conceptualization. **Ruben Ansorena Ruiz:** Writing – review & editing, Validation, Investigation, Formal analysis, Data curation. **Justus Hoffstaedt:** Writing – review & editing, Investigation, Data curation. **David Schürenkamp:** Writing – review & editing, Supervision, Project administration, Funding acquisition. **Nils Goseberg:** Writing – review & editing, Supervision, Project administration, Funding acquisition. **Antonio Jarquin Laguna:** Writing – review & editing, Supervision, Project administration, Funding acquisition. **Kurt Stockman:** Writing – review & editing, Supervision, Project administration, Funding acquisition. **Jeroen D.M. De Kooning:** Writing – review & editing, Supervision, Project administration, Funding acquisition.

## Declaration of competing interest

The authors declare the following financial interests/personal relationships which may be considered as potential competing interests: Daan P. K. Truijen reports financial support was provided by European Commission. Ruben Ansorena Ruiz reports financial support was provided by European Commission. Justus Hoffstaedt reports financial support was provided by European Commission. David Schurenkamp reports financial support was provided by European Commission. Nils Goseberg reports financial support was provided by European Commission. Antonio Jarquin Laguna reports financial support was provided by European Commission. Kurt Stockman reports financial support was provided by European Commission. Jeroen D. M. De Kooning reports financial support was provided by European Commission. If there are other authors, they declare that they have no known competing financial interests or personal relationships that could have appeared to influence the work reported in this paper.

## Acknowledgments

This research is performed in context of the ALPHEUS project, which has received funding from the European Union's Horizon 2020 research and innovation programme under grant agreement No 883553.

## Appendix A. Cavitation in pump mode

In pump mode, cavitation is pictured for four operating points. These operating points, together with their net head $h_{RPT}$, are listed in Table A.6. The pictures are shown in Fig. A.13. Note that runner 1 and runner 2 are on the right and left side of the picture, respectively. It can be seen that with increasing rotational speed, the Thoma number decreases, and the cavitation region increases. For OP1, with $\sigma = 1.46$, a small region of cavitation inception is observed at the leading edge of runner 1, with a minimal region detected at the leading edge of runner 2. Reducing to $\sigma = 1.39$ for OP2, only a small increase in the blade coverage is found. However, when reducing to $\sigma = 1.32$, the cavitating region on runner 1 has noticeably extended, with minimal indications of tip leakage cavitation observed. These effects increase for OP4 at $\sigma = 1.20$, where over half the blade surface of runner 1 is covered by a cavitating layer and the tip leakage cavitation is significant. The observations are in line with the computational fluid dynamics study in [46], although an increase in cavitation for lower Thoma numbers is not observed for runner 2.

## Appendix B. Direct torque control error

In the ABB variable-frequency drives, direct torque control (DTC) is used to convert the torque setpoints $\hat{\tau}_{m1,2}$ to the corresponding voltage vectors. An important module in the DTC controller is the estimator, which consists of an internal motor-generator model. Based on voltage and current measurements, this module estimates the machine torque and stator flux to compare it to their respective setpoints [48]. Due to inaccuracies in the internal model used in the drives, a small steady-state error exists between the torque setpoints $\hat{\tau}_{m1,2}$ and the actual (measured) machine torques $\tau_{m1,2}$. In [44], it is found that the error $\epsilon = |\hat{\tau}_m - \tau_m|$ is a function of both the magnitude of the torque setpoint and the rotational speed, with the errors being the highest in generator mode. Therefore, lookup table $\mathcal{L}$ (see Section 3.1) is populated with the expected steady-state torque setpoints $\tau^*_{m1,2}$ and power distribution $P^*_{1,2}$, instead of the actual measured torques $\tau_{m1,2}$ and powers $P_{1,2}$ during the characterization tests. However, for the validation in Section 4, the measured power response is still used.

## Data availability

Data will be made available on request.

## References


[1] International Energy Agency. Renewables 2023. Tech. rep., 2024, p. 15, URL https://www.iea.org/reports/renewables-2023.

[2] Jülch V. Comparison of electricity storage options using levelized cost of storage (LCOS) method. Appl Energy 2016;183:1594–606. http://dx.doi.org/10.1016/j.apenergy.2016.08.165.

[3] International Energy Agency. Grid-scale storage. 2024, URL https://www.iea.org/energy-system/electricity/grid-scale-storage. [Accessed 31 July 2024].

[4] European Commission. Commission Regulation (EU) 20171485: Establishing a guideline on electricity transmission system operation. Tech. rep., 2017, p. 130–6, URL https://eur-lex.europa.eu/legal-content/EN/TXT/?uri=CELEX:02017R1485-20210315.

[5] Agneholm E, Jansson EA. FCP Project Summary report. Tech. rep., European Network of Transmission System Operators for Electricity; 2017, p. 4, URL https://www.svk.se/contentassets/e5a38b7a16a443b290f5d49d42ea03c0/1—fcp-project-summary-report.pdf.

[6] Prasasti E, Aouad M, Joseph M, Zangeneh M, Terheiden K. Optimization of pumped hydro energy storage design and operation for offshore low-head application and grid stabilization. Renew Sustain Energy Rev 2024;191:114122. http://dx.doi.org/10.1016/j.rser.2023.114122.

[7] Fahlbeck J, Nilsson Ha, Salehi S, Zangeneh M, Joseph M. Numerical analysis of an initial design of a counter-rotating pump-turbine. IOP Conf Ser Earth Environ Sci 2021;774:012066. http://dx.doi.org/10.1088/1755-1315/774/1/012066.

[8] Yang W, Yang J, Guo W, Norrlund P. Response time for primary frequency control of hydroelectric generating unit. Int J Electr Power Energy Syst 2016;74:16–24. http://dx.doi.org/10.1016/j.ijepes.2015.07.003.

[9] Gezer D, Taşcı oğlu Y, Çelebioğlu K. Frequency containment control of hydropower plants using different adaptive methods. Energies 2021;14(8). http://dx.doi.org/10.3390/en14082082.

[10] Oliveira EJ, Honório LM, Anzai AH, Oliveira LW, Costa EB. Optimal transient droop compensator and PID tuning for load frequency control in hydro power systems. Int J Electr Power Energy Syst 2015;68:345–55. http://dx.doi.org/10.1016/j.ijepes.2014.12.071.

[11] Ngoma D, Mfangavo A, Masenga B. Comparative control governor systems for power and frequency optimization of an islanding off-grid small hydropower plant. Discov Energy 2025;5. http://dx.doi.org/10.1007/s43937-025-00066-8.

[12] Kumari R, Prabhakaran K, Desingu K, Chelliah TR, Sarma SVA. Improved hydroturbine control and future prospects of variable speed hydropower plant. IEEE Trans Ind Appl 2021;57(1):941–52. http://dx.doi.org/10.1109/TIA.2020.3028798.

[13] Beus M, Pandžić H. Practical implementation of a hydro power unit active power regulation based on an MPC algorithm. IEEE Trans Energy Convers 2022;37(1):243–53. http://dx.doi.org/10.1109/TEC.2021.3094059.

[14] Li C, Mao Y, Yang J, Wang Z, Xu Y. A nonlinear generalized predictive control for pumped storage unit. Renew Energy 2017;114:945–59. http://dx.doi.org/10.1016/j.renene.2017.07.055.

[15] Bulatov YN, Kryukov A, Suslov K. Group predictive voltage and frequency regulators for small hydro power plant in the context of low power quality. Renew Energy 2022;200:571–8. http://dx.doi.org/10.1016/j.renene.2022.10.017.

[16] Hoffstaedt J, Truijen D, Fahlbeck J, Gans L, Qudaih M, Laguna A, et al. Low-head pumped hydro storage: A review of applicable technologies for design, grid integration, control and modelling. Renew Sustain Energy Rev 2022;158:112119. http://dx.doi.org/10.1016/j.rser.2022.112119.

[17] Mercier T, Jomaux J, De Jaeger E, Olivier M. Provision of primary frequency control with variable-speed pumped-storage hydropower. In: 2017 IEEE manchester powerTech. Manchester, United Kingdom; 2017, p. 1–6. http://dx.doi.org/10.1109/PTC.2017.7980920.

[18] Bontemps P, Hugo N, Dujic D. Flexibility enhancements in pumped hydro storage power plants through variable speed drives. In: IECON 2020 the 46th annual conference of the IEEE industrial electronics society. 2020, p. 1820–5. http://dx.doi.org/10.1109/IECON43393.2020.9254499.

[19] Yang W, Yang J. Advantage of variable-speed pumped storage plants for mitigating wind power variations: Integrated modelling and performance assessment. Appl Energy 2019;237:720–32. http://dx.doi.org/10.1016/j.apenergy.2018.12.090.

[20] Cao R, Guo W, Qu F. Hydraulic disturbance characteristics and power control of pumped storage power plant with fixed and variable speed units under generating mode. J Energy Storage 2023;72:108298. http://dx.doi.org/10.1016/j.est.2023.108298.

[21] Merbeth (né Sarodnik) R, Schönborn B, Bruns M, Jung A. Increasing grid flexibility through ancillary services – virtual inertia and fast frequency response implementation and testing in a PSPP with double-fed induction machines. IOP Conf Ser: Earth Environ Sci 2024;1411(1):012052. http://dx.doi.org/10.1088/1755-1315/1411/1/012052.

[22] Vasudevan KR, Ramachandaramurthy VK, Venugopal G, Guerrero JM, Ekanayake JB, Tiong SK. Variable-speed PICO hydel energy storage with synchronverter control to emulate virtual inertia in autonomous microgrids. IEEE Syst J 2022;16(1):452–63. http://dx.doi.org/10.1109/JSYST.2021.3053358.

[23] Krishnakumar R. V, Vigna KR, Gomathi V, Ekanayake J, Tiong S. Modelling and simulation of variable speed pico hydel energy storage system for microgrid applications. J Energy Storage 2019;24:100808. http://dx.doi.org/10.1016/j.est.2019.100808.

[24] Márquez J, Molina M, Pacas J. Dynamic modeling, simulation and control design of an advanced micro-hydro power plant for distributed generation applications. Int J Hydrog Energy 2010;35(11):5772–7. http://dx.doi.org/10.1016/j.ijhydene.2010.02.100, 3rd Argentinean and 2nd Latin American Congress inHydrogen and Sustainable Energy Sources.

[25] Gao J, Dai L, Liu X, Du X, Luo D, Huang S. Variable-speed hydropower generation: System modeling, optimal control, and experimental validation. IEEE Trans Ind Electron 2021;68(11):10902–12. http://dx.doi.org/10.1109/TIE.2020.3031528.

[26] Zhou Q, Luo D, Dai L, Wu B, Luo H. MPPT control strategy of variable speed hydropower system based on improved fuzzy control. In: 2021 IEEE 4th student conference on electric machines and systems. 2021, p. 1–6. http://dx.doi.org/10.1109/SCEMS52239.2021.9646103.

[27] Borkowski D. Maximum efficiency point tracking (MEPT) for variable speed small hydropower plant with neural network based estimation of turbine discharge. IEEE Trans Energy Convers 2017;32(3):1090–8. http://dx.doi.org/10.1109/TEC.2017.2690447.

[28] Atta KT, Johansson A, Cervantes MJ, Gustafsson T. Phasor extremum seeking and its application in kaplan turbine control. In: 2014 IEEE conference on control applications. 2014, p. 298–303. http://dx.doi.org/10.1109/CCA.2014.6981362.

[29] Dreyer M, Nicolet C, Alligné S, Seydoux M, Jung A, Cordeiro D. Pushing the envelope of ancillary services with variable speed technology. IOP Conf Ser: Earth Environ Sci 2022;1079(1):012110. http://dx.doi.org/10.1088/1755-1315/1079/1/012110.

[30] Reigstad TI, Uhlen K. Nonlinear model predictive control of variable speed hydropower for provision of fast frequency reserves. Electr Power Syst Res 2021;194:107067. http://dx.doi.org/10.1016/j.epsr.2021.107067.

[31] Reigstad TI, Uhlen K. Variable speed hydropower for provision of fast frequency reserves in the nordic grid. IEEE Trans Power Syst 2021;36(6):5476–85. http://dx.doi.org/10.1109/TPWRS.2021.3078098.

[32] Mennemann J-F, Marko L, Schmidt J, Kemmetmüller W, Kugi A. Nonlinear model predictive control of a variable-speed pumped-storage power plant. IEEE Trans Control Syst Technol 2021;29(2):645–60. http://dx.doi.org/10.1109/TCST.2019.2956910.

[33] Xu Z, Deng C, Yang Q. A primary frequency control strategy for variable-speed pumped-storage plant in generating mode based on adaptive model predictive control. Electr Power Syst Res 2023;221:109356. http://dx.doi.org/10.1016/j.epsr.2023.109356.

[34] Badwe AS, Patwardhan RS, Shah SL, Patwardhan SC, Gudi RD. Quantifying the impact of model-plant mismatch on controller performance. J Process Control 2010;20(4):408–25. http://dx.doi.org/10.1016/j.jprocont.2009.12.006.

[35] Dixon S, Hall C. Chapter 2 - dimensional analysis: Similitude. In: Fluid mechanics and thermodynamics of turbomachinery (seventh edition). 7th ed.. Boston: Butterworth-Heinemann; 2014, p. 39–67. http://dx.doi.org/10.1016/B978-0-12-415954-9.00002-4.

[36] Kim J-H, Cho B-M, Kim S, Kim J-W, Suh J-W, Choi Y-S, et al. Design technique to improve the energy efficiency of a counter-rotating type pump-turbine. Renew Energy 2017;101:647–59. http://dx.doi.org/10.1016/j.renene.2016.09.026.

[37] Fahlbeck J, Nilsson Ha, Salehi S. Flow characteristics of preliminary shutdown and startup sequences for a model counter-rotating pump-turbine. Energies 2021;14:3593. http://dx.doi.org/10.3390/en14123593.
[38] Fahlbeck J, Nilsson H, Salehi S. Surrogate based optimisation of a pump mode startup sequence for a contra-rotating pump-turbine using a genetic algorithm and computational fluid dynamics. J Energy Storage 2023;62:106902. http://dx.doi.org/10.1016/j.est.2023.106902.
[39] Hoffstaedt J, Ansorena Ruiz R, Schürenkamp D, Jarquin Laguna A, Goseberg N. Experimental setup and methods for a novel low-head pumped storage system. In: 7th offshore energy & storage symposium. IET Digital Library; 2023, p. 341–8. http://dx.doi.org/10.1049/icp.2023.1589.
[40] Truijen DP, De Kooning JD, Stockman K. Drivetrain architectures for a mechanically decoupled contra-rotating reversible pump-turbine. In: 2021 IEEE/aSME international conference on advanced intelligent mechatronics. 2021, p. 7–12. http://dx.doi.org/10.1109/AIM46487.2021.9517403.
[41] Wang H, Wang F, Wang C, Wang B, Li C, Li D. A prospective assessment of scale effects of energy conversion in ultra-low-head pumped hydro energy storage units. Energy Convers Manage 2024;315:118798. http://dx.doi.org/10.1016/j.enconman.2024.118798.
[42] Ida T. Analysis of scale effects on performance characteristics of hydraulic turbines. J Hydraul Res 1990;28(1):93–104. http://dx.doi.org/10.1080/00221689009499149.
[43] Junginger J. Feasibility of transient model tests in a closed-loop test rig with the example of a reversible pump turbine [Ph.D. thesis], Institut für Strömungsmechanik und Hydraulische Strömungsmaschinen, Universität Stuttgart; 2023, p. 17–20,109–110.
[44] Truijen DP, Hoffstaedt JP, Fahlbeck J, Jarquin-Laguna A, Nilsson H, Stockman K, De Kooning JD. Hardware-in-the-loop emulator test-setup for a dual-rotor contra-rotating pump-turbine. In: 13th international conference on power electronics, machines and drives. 2024, p. 1–8. http://dx.doi.org/10.1049/icp.2024.2140.
[45] IEC 60193:1999 v2.0, Hydraulic turbines, storage pumps and pump-turbines - Model acceptance tests. Tech. rep., International Electrotechnical Commission; 1999.
[46] Fahlbeck J, Nilsson H, Arabnejad MH, Salehi S. Performance characteristics of a contra-rotating pump-turbine in turbine and pump modes under cavitating flow conditions. Renew Energy 2024;237:121605. http://dx.doi.org/10.1016/j.renene.2024.121605.
[47] Truijen DP, Hoffstaedt JP, Fahlbeck J, Jarquin Laguna A, Nilsson Ha, Stockman K, et al. Impact of dual variable speed and inlet valve control on the efficiency and operating range of low-head contra-rotating pump-turbines. IEEE Access 2024;12:86854–68. http://dx.doi.org/10.1109/ACCESS.2024.3416679.
[48] drives A. Technical guid No.1: Direct torque control - the world's most advanced AC drive technology. C, Asea Brown Boveri; 2011, URL https://library.e.abb.com/public/14f3a3ad8f3362bac12578a70041e728/ABB_Technical_guide_No_1_REVC.pdf.
[49] 50hertz, Amprion, Tennet, Transnet bw. Tech. rep., In: Prequalification Process for Balancing Service Providers (FCR, aFRR, mFRR) in Germany ("PQ conditions"), vol. 1.04, Regelleistung.net; 2022, URL https://www.regelleistung.net/Portals/1/downloads/regelenergieanbieter_werden/pr%C3%A4qualifikationsbedingungen/PQ%20Bedingungen%20-%2003.06.2022%20(englisch).pdf?ver=4rD5rRjAmi_tqY0oI3Q2Mw%3d%3d.
[50] Balancing Capacity - Data in second resolution. Netztransparenz.de; 2024, URL https://www.netztransparenz.de/en/Balancing-Capacity/Balancing-Capacity-data/Data-in-second-resolution. [Accessed 10 April 2024].
[51] Wang H, Gong J. Dynamic analysis of coupling misalignment and unbalance coupled faults. J Low Freq Noise Vib Act Control 2019;38(2):363–76. http://dx.doi.org/10.1177/1461348418821582.
[52] Saarinen L, Norrlund P, Yang W, Lundin U. Allocation of frequency control reserves and its impact on wear and tear on a hydropower fleet. IEEE Trans Power Syst 2018;33(1):430–9. http://dx.doi.org/10.1109/TPWRS.2017.2702280.
[53] Cassano S, Sossan F. Stress-informed control of medium- and high-head hydropower plants to reduce penstock fatigue. Sustain Energy Grids Networks 2022;31:100688. http://dx.doi.org/10.1016/j.segan.2022.100688.
[54] Betti A, Crisostomi E, Paolinelli G, Piazzi A, Ruffini F, Tucci M. Condition monitoring and predictive maintenance methodologies for hydropower plants equipment. Renew Energy 2021;171:246–53. http://dx.doi.org/10.1016/j.renene.2021.02.102.